International Journal for Multiscale Computational Engineering, 6(5)483–498(2008)

Subject-Specific p-FE Analysis of the Proximal Femur Utilizing Micromechanics-Based Material Properties

Zohar Yosibash & Nir Trabelsi

Department of Mechanical Engineering, Ben-Gurion University, Beer-Sheva 84105, Israel

Christian Hellmich

Institute for Mechanics of Materials and Structures, Vienna University of Technology, A-1040 Vienna, Austria

ABSTRACT

Novel subject-specific high-order finite element models of the human femur based on computer tomographic (CT) data are discussed with material properties determined by two different methods, empirically based and micromechanics based, both being determined from CT scans. The finite element (FE) results are validated through strain measurements on a femur harvested from a 54-year-old female. To the best of our knowledge, this work is the first to consider an inhomogeneous Poisson ratio and the first to compare results obtained by micromechanics-based material properties to experimental observations on a whole organ. We demonstrate that the FE models with the micromechanics-based material properties yield results which closely match the experimental observations and are in accordance with the empirically based FE models. Because the p-FE micromechanics-based results match independent experimental observations and may provide access to patient-specific distribution of the full elasticity tensor components, it is recommended to use a micromechanics-based method for subject-specific structural mechanics analyses of a human femur.

KEYWORDS

proximal femur, finite element analysis, p-FEM, computed tomography (CT), bone biomechanics, continuum micromechanics, X-ray attenuation

*Address all correspondence to zohary@bgu.ac.il

1. INTRODUCTION

Patient-specific finite element (FE) analyses of the human femur have matured over the past decade. The geometrical description of the bone is determined by manipulating computer tomographic (CT) scans. The elastic material properties are determined based on a regression function between the Hounsfields units (HUs) from CT (related to X-ray attenuation coefficients and therefore mineral density) and the inhomogeneous material behavior according to *empirical connections*. A major issue challenging the reliability of such computations seems to be the association between the HU and material properties, being anisotropy and inhomogeneous throughout the bone. Frequently, isotropy of the bone tissue is assumed [1–6], while the material properties are still inhomogeneously distributed across the organ. The isotropic material properties are determined by regression functions between HU from CT or mass density values on the one hand, and values for (isotropic) Young's modulus on the other, while the Poisson ratio is assumed to be a constant. There are many such empirical connections, which are obtained by performing tests on small pieces taken from different locations along the whole bone. Thereby, the isotropic Young's modulus E of cortical or trabecular bone may be associated with bone apparent density (ρ_{app}) or bone ash density (ρ_{ash}) [7–11]. Bone's density, in turn, can be correlated to HUs, resulting in an $E(HU)$ relationship (see, e.g., [10, 12]). Also, the use of different direct *still empirical* connections $E(HU)$ in FE models has been thoroughly investigated [1–4, 6, 13].

The validity and reliability of such $E(HU)$ connections in FE simulations can be improved with respect to at least two aspects: First, transverse isotropy of the cortical material properties, instead of isotropy, can be considered in the FE analysis. While this has been somewhat addressed in [8, 11, 14], herein we report on the feasibility of such an approach, but mostly focus on a second aspect of possible improvement: The replacement of empirical HU-elastic property relations by relations derived from the microstructure and vascular porosity within a piece (or representative volume element) of cortical or trabecular bone. The porosity is accessed through average rules for X-ray attenuation coefficients and basic biochemical knowledge on bones. Such an approach, delivering naturally nonconstant Poisson ratios, has proved beneficial in the case of a human mandible simulation [15]. In [15], the influence of inhomogeneous and anisotropic material properties (derived from an experimentally validated micromechanics model [16]) on the overall structural behavior of the organ has been clearly shown. Still, neither has this approach been applied to other organ systems, nor has the structural response predicted by such micromechanics-based FE analysis been compared to experimental observations at the macroscale.

This is exactly the focus of the present article. We herein improve the p-FE analyses of the proximal femur reported in [5, 13] by considering inhomogeneous micromechanics-based material properties. In [5, 13], inhomogeneous *empirically based* Young's modulus distributions were defined with a constant Poisson's ratio, independently of the FE mesh. Herein, a continuum micromechanics-based model is applied for identification (from QCT scans) of longitudinal Young's modulus and (varying) transverse Poisson's ratio, both being (nonempirical) functions of the HU. The strains and displacements predicted by the new p-FE simulations are compared to experimental in vitro observations on the organ. While the bulk of these simulations are based on the longitudinal Young's modulus and the transverse Poisson's ratio only (assuming isotropic material behavior), we also provide first simulations incorporating anisotropic material properties.

2. MECHANICAL EXPERIMENTS AND FE MODELS

A fresh-frozen femur was defrosted, CT-scanned, and thereafter exposed to in vitro experiments during which displacements, loads, and strains were measured. In the following, the experimental procedure is detailed together with the steps followed for the generation of the FE model and assignment of material properties.

2.1 Experiments, CT Scans, and Strain Measurements

Mechanical experiments were performed on a fresh-frozen femur of a 54-year-old female donor. The

femur was CT scanned, strain gauges (SGs) were bonded on its surface, and thereafter, several mechanical tests were performed on it (details are provided in [13]). During the CT scan, calibration phantoms were placed close to the bone, used thereafter to estimate the inhomogeneous mineral density in the bone. During the experiments, we measured the vertical and horizontal displacements of the femoral head, and also the output of the strain gauges at the surface of the proximal femur, at the inferior and superior parts of the femoral neck and on the medial and lateral femoral shaft. The experiments refer to a simple stance position configuration in which the femur is loaded through its head while it is inclined at four different inclination angles (0°,7°,15°, and 20°), as shown in Fig. 1. Strains and head displacements are quantitatively reported in [13].

2.2 Finite Element Models

Structural models mimicking the experiments were created in the framework of the p-version of the FE method. In short, the following steps were realized (see Fig. 2 and [5] for further details): The geometry of the femur was extracted from QCT slices and divided into cortical and trabecular regions. Exterior, interface, and interior boundaries were traced at each slice and $x - y$ arrays were generated, each representing different boundaries of a given slice. A smoothing algorithm was applied on these arrays which generate smooth closed splines used for the solid body generation. The solid body was meshed by an auto-mesher with tetrahedral elements using p-FE StressCheck[1] code. The surfaces of the bone are accurately represented in the FE model by using the blending mapping method.

The material properties at each integration point (there are 512 Gauss points per tetrahedral element) were directly extracted from the CT scan; that is, the CT data were converted to a 3-D array describing the location of each pixel, and the Young's modulus value was assigned to each voxel by means of two different approaches (see Sections 2.3 and 2.4). From these values, the Gauss point-specific values are defined by means of a weighted point average method. Eight points (creating a closed box) around the Gauss point of interest were identified directly from the 3-D array (see Fig. 3), and the value at the Gauss point was determined according to its relative distance from each CT data point (pixel).

The boundary conditions applied to the FE model reflect the experimental setup: The distal face was fully constrained, and at the planar face cut out of the head, a load of 1000N was applied, directed according to four different inclination angles (0°, 7°, 15°, and 20°) (see Fig. 1).

2.3 Empirical Determination of Voxel-Specific (Isotropic) Young's Modulus

Recently, different empirical relationships between Young's modulus and HU, while using a constant Poisson's ratio, were considered for FE analyses with inhomogeneous, isotropic elastic properties of three different human femurs [5, 13]. The performance of these relationships, validated through experimental measurements on the three simulated organs, was markedly different, revealing comparable superiority in terms of reliable and accurate predictions of Keyak's empirical relationship [12]. This relationship is between the longitudinal Young's modulus and HU, in combination with a constant Poisson's ratio $\nu = 0.3$.

Based on these findings, we herein determine (as in [4, 5]) the Young's modulus $E(\boldsymbol{x})$ ($\boldsymbol{x}$ denotes the position of a given point or voxel in the bony organ) as follows: HUs were computed directly from the CT slices. A moving average algorithm was applied with a predefined cubic volume of 3×3 mm^3. Averaged HUs were converted to an equivalent mineral density ρ_{EQM} [g/cm^3]. The linear relation ρ_{EQM}(HU) was determined by calibration phantoms; it reads as

$$\rho_{EQM} = 0.81 \cdot HU - 11 \quad [\mathrm{g/cm^3}], \qquad \mathrm{R}^2 = 0.99 \quad (1)$$

Since we use Young's modulus as a function of ash density (ρ_{ash}), the following relations from [12] were used:

$$\rho_{Ash} = 1.22 \cdot \rho_{EQM} + 0.0523 \qquad [\mathrm{g/cm^3}] \quad (2)$$

$$E_{Cort} = 10200 \cdot \rho_{Ash}^{2.01} \qquad [\mathrm{MPa}] \quad (3)$$

$$E_{Trab} = 5307 \cdot \rho_{Ash} + 469 \qquad [\mathrm{MPa}] \quad (4)$$

[1] StressCheck is a trademark of Engineering Software Research and Development, Inc., St. Louis, MO.

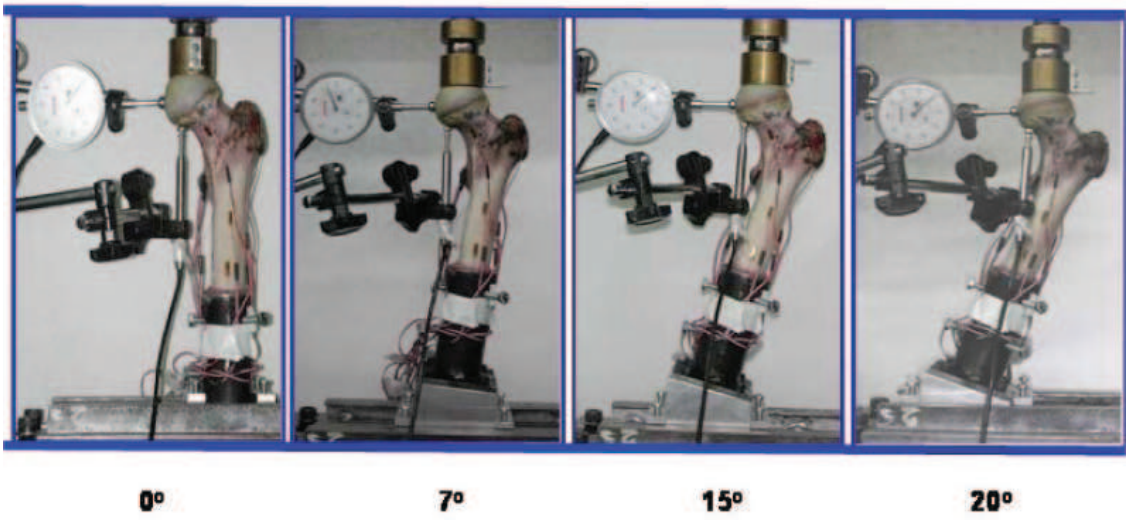

FIGURE 1. Experiments on the fresh-frozen bone at different inclination angles

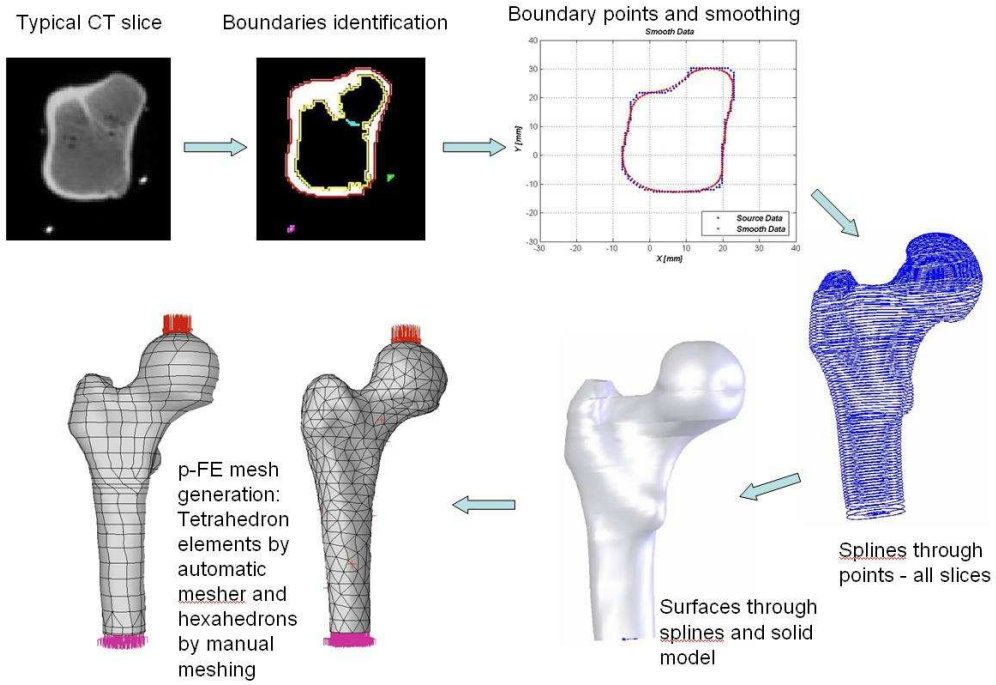

FIGURE 2. The flow chart for generating the p-FE model

2.4 Micromechanics-Based Determination of Voxel-Specific (Anisotropic) Young's Moduli and Poisson's Ratios

Micromechanics-based determination of voxel-specific material properties is based on two consecutive steps [15]:

- Based on voxel average rules for the attenuation coefficients [17], we assign to each voxel the volume fraction occupied by water (marrow) and that occupied by solid bone matrix.
- By means of a micromechanical model for bone based on stiffness properties of solid bone ma-

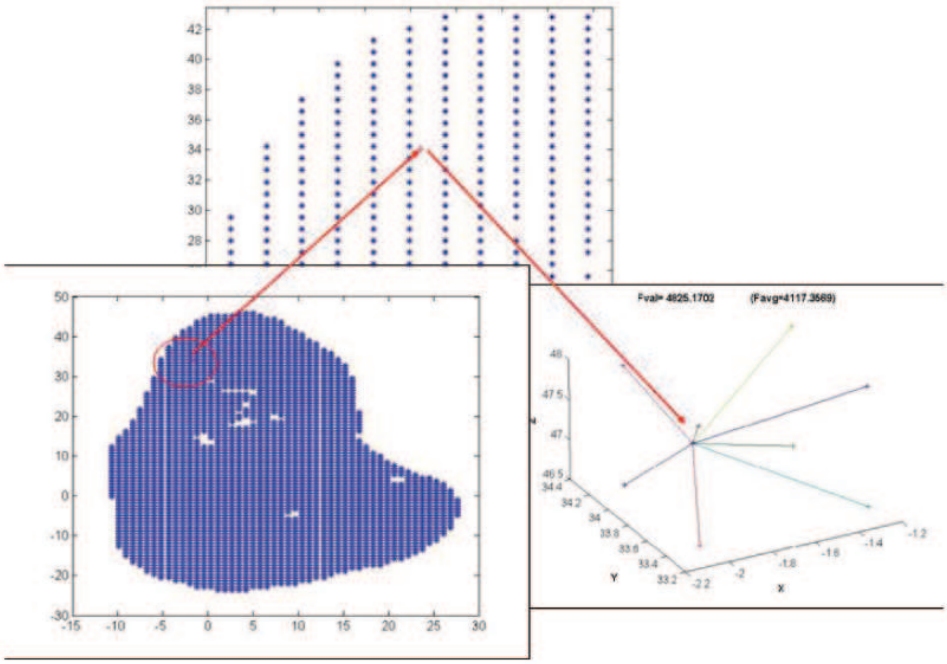

FIGURE 3. Weighted point average: Identified is the point in the 3-D array, and the Gauss point value is set as the average according to its surroundings

trix and of water, in the line of [18, 19], we convert the aforementioned volume fractions into voxel-specific orthotropic (and also transversely isotropic) stiffness tensor components corresponding to a base frame coinciding with the principal material directions.

More specifically, the voxel-specific HU are related to the attenuation coefficients of the macroscopic (porous) bone material inside a millimeter-sized voxel, μ, and of water, μ_{H_2O}, respectively:

$$HU(\boldsymbol{x}) = \frac{\mu(\boldsymbol{x})}{\mu_{H_2O}} \times 1000 - 1000 \tag{5}$$

where $\boldsymbol{x}$ labels the position of the individual voxels. The attenuation coefficients for a bone which is composed of two constituents; (1) the water-filled vascular pore space and (2) the (extravascular) solid bone matrix, can be expressed with high accuracy in terms of the mass attenuation coefficients of their single constituents [15, 17, 20]:

$$\mu = \mu_{BM} f_{BM} + \mu_{H_2O} f_{H_2O} \tag{6}$$

where f_i is the volume fraction of constituent i.

The solid bone matrix is composed of mineral (hydroxyapatite), collagen, and water (with some noncollageneous organics) (e.g., [21, 22]). The chemical composition of the solid bone matrix, for example, its mineral/collagen/water content, varies from species to species and from one anatomical location to another [22–24]. It also varies at a small scale of some microns or of tens of microns [25]. However, within one whole bone of one species (e.g., human iliac crest, iliac bone, vetebra, femur, radius, mandible), the chemical composition *(mineral/collagen/water content) of the average solid bone matrix inside a millimeter-sized voxel remains constant, both in space (i.e., across all voxels representing the whole bone) and in time (i.e., during aging, from early adulthood on)*. This constancy is evidenced through numerous experimental results, from computerized quantitative contact microradiography [25], quantitative backscattered electron imaging [26], Raman spectroscopy [27], or Synchroton microcomputer tomography [28] (see [15] for a detailled discussion). Such voxel-invariant chemical composition of the solid bone matrix, that is, of

its mineral/collagen/water content, implies voxel-invariance of its mass attenuation coefficient μ_{BM}. Hence, in our case, Eq. (6) can be specified as

$$\mu = \mu_{BM}(1-\phi) + \mu_{\mathrm{H_2O}}\phi \tag{7}$$

with the vascular porosity ϕ as the volume fraction of the vascular pore space with pores of tens to hundreds of microns in size. When multiplied by $(1000/\mu_{\mathrm{H_2O}})$, Eq. (7) can be written in terms of the HU, according to Eq. (5):

$$HU = HU_{BM}(1-\phi) \tag{8}$$

with $HU_{BM} = 1000\mu_{BM}/\mu_{\mathrm{H_2O}} - 1000$. Once HU_{BM} is known, Eq. (8) provides a link between the voxel-specific HU known from the CT scan and the voxel-specific vascular porosity which will enter the micromechanical model (11). For determination of HU_{BM}, we consider standard statistical characteristics of the HU values occurring in the entire CT scans of the human femur, namely, the frequency distribution and the cumulative frequency plot (see Fig. 4).

According to Eq. (5), $HU = 0$ relates to pure water so that the values at the lower end of the frequency plot of Fig. 4(b) refer to very porous trabecular bone, with a vascular porosity close to 100%. At the upper end of the HU values, we realize from the cumulative frequency plot of Fig. 4(b) that the range beyond 1600 is occupied by negligibly few values. Therefore the value of 1600 can be identified as the one related to vanishing vascular porosity, $\phi \approx 0$, that is, to "perfectly" compact bone, to solid bone matrix $HU_{BM} = 1600$. With this value at hand, the spatial distribution of the vascular porosity can be determined from the HU values through rearrangement of Eq. (8):

$$\phi(\boldsymbol{x}) = \begin{cases} \dfrac{HU_{BM} - HU(\boldsymbol{x})}{HU_{BM}} & \forall\ HU \le 1600 \\ 0 & \text{otherwise} \end{cases} \tag{9}$$

The distribution of ϕ as a function of the (macroscopic) position vector with millimeter resolution, defining the location in the organ, allows one to determine the fields of elastic constants throughout the organ, as described next.

The elastic properties of the solid bone matrix depend mostly on its chemical composition (mineral/collagen/water content) since the morphological patterns [29] built up over various length scales by mineral crystals and collagen molecules are virtually universal across the bone tissues found in the vertebrate kingdom [16, 19]. Hence time- and voxel-invariant mineral and collagen and water contents of the solid bone matrix of one species-specific whole bone (see discussion below (6)) result in time- and voxel-invariant elastic properties of the solid

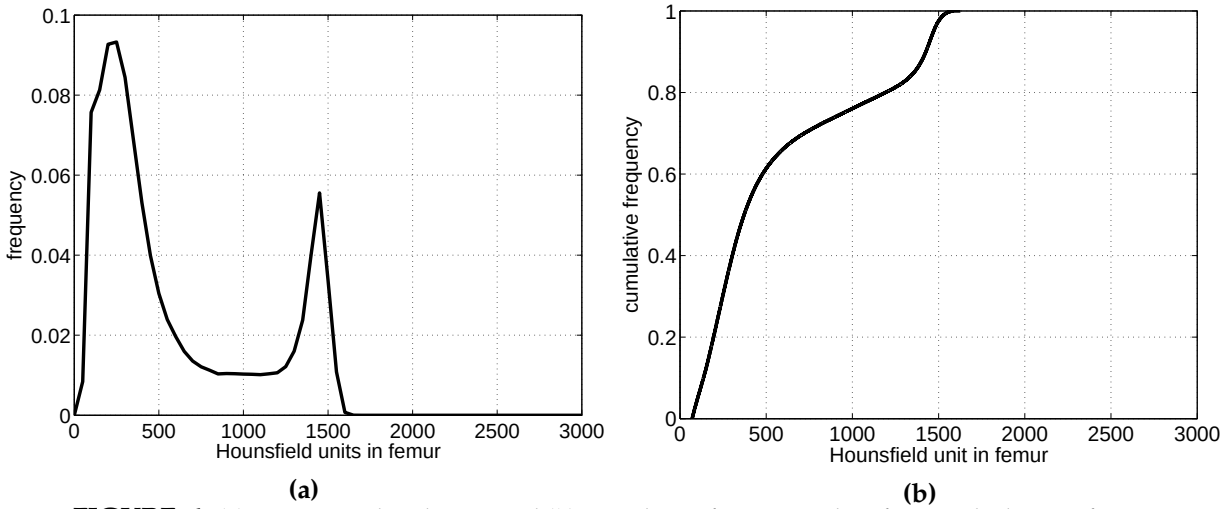

FIGURE 4. (**a**) Frequency distribution and (**b**) cumulative frequency plot of HU in the human femur

bone matrix found within one whole bone. The corresponding stiffness tensor, $\mathbb{C}_{BM}$, is accessible through ultrasonic tests on samples from a human femur, with 2.25 MHz frequency, made by [30]. Such ultrasonic waves with a wave length λ of typically 1 mm "detect" elastic properties at a scale where stresses and strains become quasihomogeneous, that is, at a scale considerably lower than λ, which refers to the extravascular bone matrix with a characteristic length of roughly 100 μm (see [16] for corresponding acoustomechanical details). Hence 2.25 MHz-ultrasonics delivers bone matrix elastic properties, irrespective of the actual vascular porosity at one scale above. The corresponding nonzero components $C_{BM,ijkl}$ of the orthotropic elasticity tensor of the (extravascular) bone matrix of a human femur, $\mathbb{C}_{BM}^{orth}$, are reported by [16, 30]:

$$\mathbb{C}_{BM}^{exp} = \begin{pmatrix} C_{1111} & C_{1122} & C_{1133} & 0 & 0 & 0 \\ C_{1122} & C_{2222} & C_{2233} & 0 & 0 & 0 \\ C_{1133} & C_{2233} & C_{3333} & 0 & 0 & 0 \\ 0 & 0 & 0 & 2C_{2323} & 0 & 0 \\ 0 & 0 & 0 & 0 & 2C_{1313} & 0 \\ 0 & 0 & 0 & 0 & 0 & 2C_{1212} \end{pmatrix} \quad (10)$$

$$= \begin{pmatrix} 18.5 & 10.3 & 10.4 & 0 & 0 & 0 \\ 10.3 & 20.8 & 11.0 & 0 & 0 & 0 \\ 10.4 & 11.0 & 28.4 & 0 & 0 & 0 \\ 0 & 0 & 0 & 12.9 & 0 & 0 \\ 0 & 0 & 0 & 0 & 11.5 & 0 \\ 0 & 0 & 0 & 0 & 0 & 9.3 \end{pmatrix}$$

In Eq. (10), 1 refers to the radial, 2 refers to the circumferential, and 3 refers to the axial (longitudinal) direction of the bone material.

Water is known to have only bulk elastic stiffness, $\mathbb{C}_{\mathrm{H_2O}} = \kappa_{\mathrm{H_2O}}\mathbb{J}$, with the bulk modulus $\kappa_{\mathrm{H_2O}} = 2.3$ GPa [31] and $\mathbb{J}$ as the volumetric part of the fourth-order identity tensor, with components $J_{ijkl} = \frac{1}{3}\delta_{ij}\delta_{kl}$.

At a length scale of several hundred microns to several millimeters, the porous medium bone is represented as a two-phase composite material (see Fig. 5) consisting of (1) a solid matrix and (2) the water-filled vascular pore space. Both the morphology of the pore space, here approximated as cylindrical inclusions in a solid matrix, as supported by experiments in [16, 19], and the anisotropy of the solid bone matrix itself, shown, for example, by ultrasonics [32, 33] or nanoindentation [34–36], govern the anisotropy of the overall "effective" elastic properties at the microstructural (= macroscopic = voxel-related) level of bone. The voxel-specific, orthotropic effective stiffness $\mathbb{C}_{eff}$ can be expressed in the framework of Eshelby problem–based continuum micromechanics [37] by considering a solid matrix with (interacting) cylindrical inclusions (standardly referred to as a Mori-Tanaka scheme [38, 39]):

$$\begin{aligned} \mathbb{C}_{eff} = & \{\phi\mathbb{C}_{\mathrm{H_2O}} : [\mathbb{I} + \mathbb{P}_{cyl} : (\mathbb{C}_{\mathrm{H_2O}} - \mathbb{C}_{BM})]^{-1} \\ & + (1-\phi)\mathbb{C}_{BM}\} : \{\phi[\mathbb{I} + \mathbb{P}_{cyl} : (\mathbb{C}_{\mathrm{H_2O}} - \mathbb{C}_{BM})]^{-1} \\ & + (1-\phi)\mathbb{I}\}^{-1} \end{aligned} \quad (11)$$

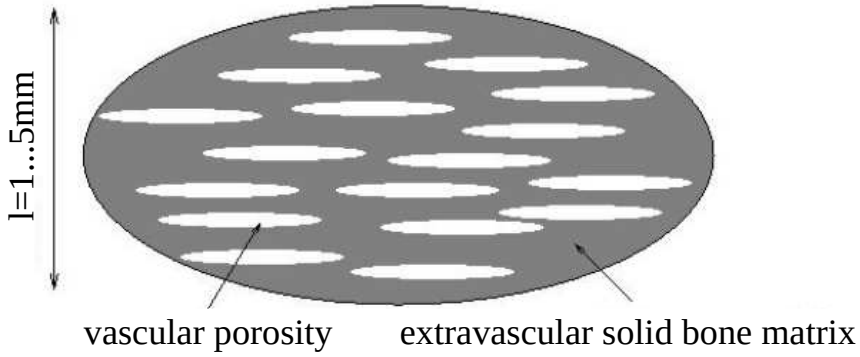

FIGURE 5. Micromechanical representation of bone material [15] inside one voxel: Prolate (cylindrical) pores are randomly embedded into an orthotropic solid bone matrix, whose axial material direction is aligned with the pores

where $\mathbb{I}$ is the fourth-order unity tensor having components $I_{ijkl} = (\delta_{ik}\delta_{jl} + \delta_{il}\delta_{jk})/2$, $\delta_{ij} = 1$ for $i = j$, zero otherwise; and with $\mathbb{P}_{cyl}$ as the fourth-order Hill tensor accounting for the cylindrical pore shape in a matrix of stiffness $\mathbb{C}_{BM}$. It reads [15, 40, 41]

$$\mathbb{P}_{cyl} = \frac{1}{2\pi}\int_0^{2\pi} \mathbb{B}(\Phi, \Theta = \frac{\pi}{2})d\Phi \tag{12}$$

with the fourth-order tensor $\mathbb{B}$;

$$\begin{aligned} \mathbb{B} &= \boldsymbol{\xi} \overset{s}{\otimes} \boldsymbol{K}^{-1} \overset{s}{\otimes} \boldsymbol{\xi} = \boldsymbol{\xi} \overset{s}{\otimes} \bar{\boldsymbol{G}} \overset{s}{\otimes} \boldsymbol{\xi} \\ B_{ijkl} &= \frac{1}{4}(\xi_i \bar{G}_{jk} \xi_l + \xi_j \bar{G}_{ik} \xi_l + \xi_i \bar{G}_{jl} \xi_k + \xi_j \bar{G}_{il} \xi_k) \end{aligned} \tag{13}$$

with the symmetrized dyadic product $\overset{s}{\otimes}$ and $\bar{\boldsymbol{G}}$ as the inverse of the acoustic tensor $\boldsymbol{K}$:

$$\boldsymbol{K} = \boldsymbol{\xi} \cdot \mathbb{C}_{BM} \cdot \boldsymbol{\xi}, \qquad K_{jk} = \xi_i C_{BM,ijkl} \xi_l \tag{14}$$

where $\boldsymbol{\xi}$ is the outward unit vector on the surface of a unit sphere (located in the middle of the cylindrical inclusion):

$$\boldsymbol{\xi} = \sin\Theta\cos\Phi \boldsymbol{e}_1 + \sin\Theta\sin\Phi \boldsymbol{e}_2 + \cos\Theta \boldsymbol{e}_3 \tag{15}$$

and with the Euler angles Θ and Φ relating $\boldsymbol{\xi}$ to an orthonormal basis $\boldsymbol{e}_1$, $\boldsymbol{e}_2$, and $\boldsymbol{e}_3$, situated in the origin of the sphere.

Use of Eq. (9) in Eq. (11) yields micromechanics-based relations between HU and the components of the voxel-specific orthotropic stiffness tensors (see next section for numerical evaluations). Averaging of these stiffness tensors over all transverse directions according to [15, 42] yields transversely isotropic approximations of these stiffness tensors, used in Section 3.3.

We are left with the question of how the material directions of the anisotropic bone material are defined at each voxel, throughout the entire organ. For the case of a human mandible, experimental and conceptual evidence demonstrates that material directions would follow the organ's geometry and internal coherent structures inside the organ [43], and one could expect that similar conclusions would hold for a human femur. Herein, however, we only slightly touch this aspect, and for consistency with previous studies using empirically based $E_{longitudinal}(HU)$, together with the fact that the femur under the considered load cases resembles a composite beam structure, we take the axial Young's modulus E_3 and the "axial" Poisson's ratio ν_{23} as the key material parameters in the isotropic FE analyses.

We also consider transversely isotropic material properties, but only in the shaft region, where the axial, circumferential, and radial directions can be directly defined on the geometrical concept of the shaft being considered as a (hollow) structural cylinder. The relevance of these simplifications will be highlighted by comparison of FE results with the strain and displacement measurements. Fully anisotropic *and* inhomogeneous material property distributions across the femoral head are beyond the scope of this manuscript — they probably evoke significant geometrical and topological challenges, which we reserve for research work to be resolved at a later point in time.

3. RESULTS

3.1 Comparison of Material Properties

The micromechanics-based longitudinal Young modulus $E_{longitudinal}(HU)$ relation is quasilinear, whereas the empirically based relation is nonlinear (see Fig. 6). To visualize the differences between the longitudinal Young modulus determined by the micromechanics-based model and the empirically based model throughout the bone, we consider a typical cut and present on it the variation of $E_{longitudinal}$ and the variation of the Poisson ratio ν (micromechanics-based model only) (see Fig. 7 and 8).

The micromechanics-based model predicts a very similar longitudinal Young modulus variation compared to the empirically based model, with a slightly smaller values but similar distribution. The Poisson ratio, on the other hand, is clearly non-constant and most probably represents reality much better.

3.2 FE Results Using Isotropic Inhomogeneous Material Properties Compared to Experimental Observations

We assigned to the p-FE models isotropic inhomogeneous material properties: For the empirically based models, Young's modulus is assigned according to Eq. (4) with $\nu = 0.3$, whereas for the micromechanics-based model, the longitudinal

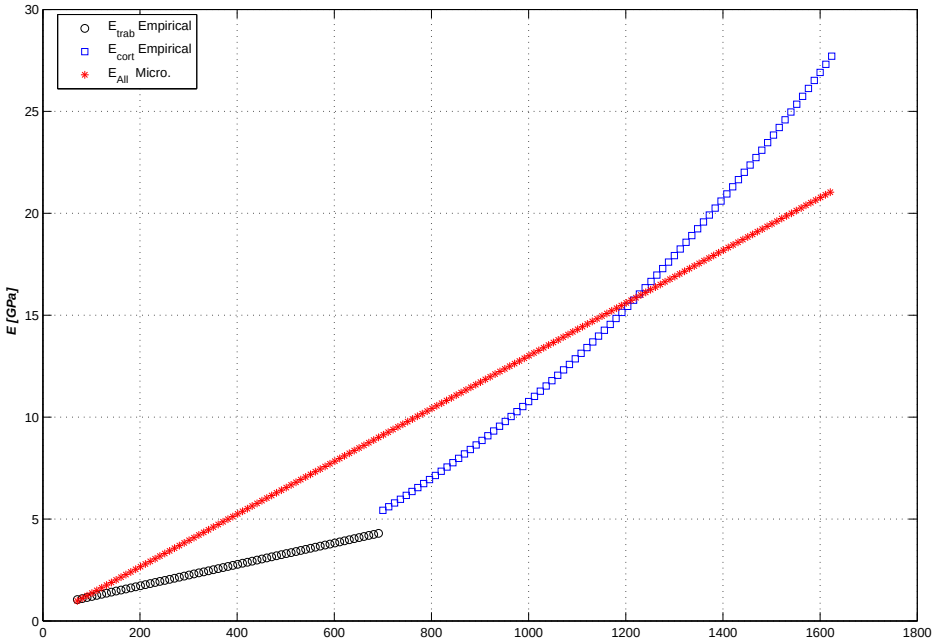

FIGURE 6. Longitudinal $E(HU)$ relation for the micromechanics-based and empirically based models

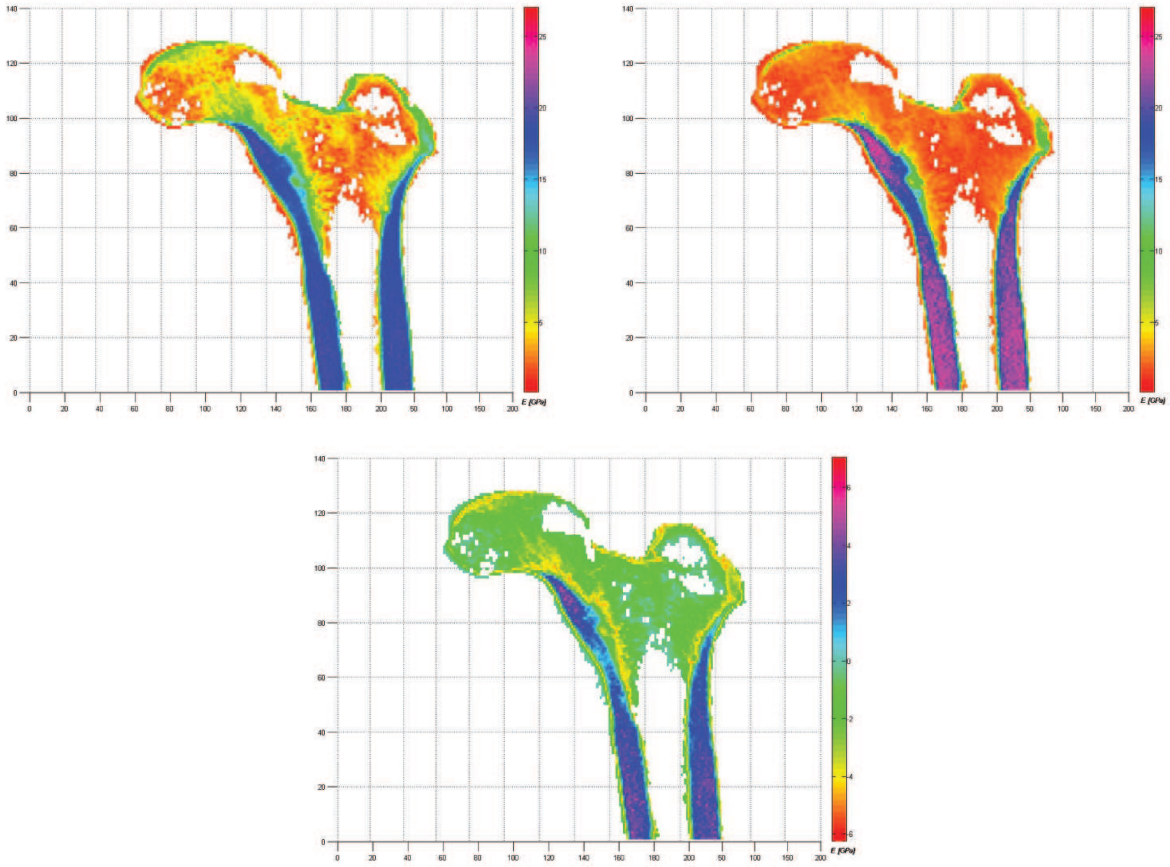

FIGURE 7. (top) Longitudinal Young modulus in a typical cut through the bone. Micromechanics-based (left) and empirically based (right). (bottom) Difference between micromechanics-based and empirically based estimated E

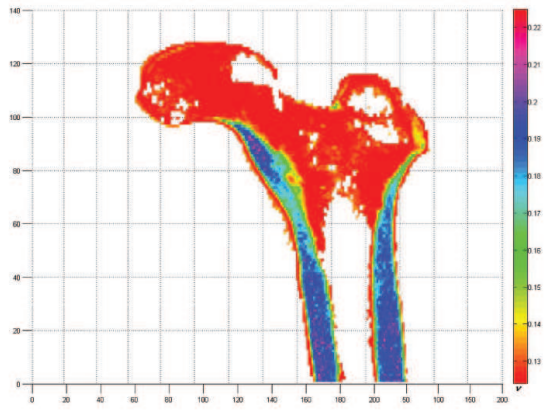

FIGURE 8. Poisson ratio variation based on the micromechanics model

Young modulus E_3 and the "axial" Poisson ratio ν_{23} is used. FE analyses of four models describing the bone loaded at different inclination angles were performed. For the verification of the models' results, we increased the polynomial degree until convergence in energy norm, strains, and displacements was attained (see [5, 13]). The converged FE results were compared to the experimental observations at nine different points: (POI1, POI3, POI8, POI10-13), horizontal and vertical displacement of the femur's head, and seven SG locations that were measured in the experiment. Results of the two different FE models (with empirical-versus micromechanics-based material properties) were compared at 16 points throughout the organ, as shown in Fig. 9.

To obtain a qualitative comparison between the results, we show in Fig. 10 the longitudinal strain ε_{zz} in the bone at $0°$ when loaded by a $1000N$. One may observe the very good correlation between the empirically based and micromechanics-based FE results.

Figure 11 presents a comparison with the experimental observations: We consider strains and displacements at the nine POIs using the two material representation strategies (empirical- and micromechanics-based) for the four different experiments at inclination angles $0°$, $7°$, $15°$, and $20°$.

A very good correlation is obtained between the predicted and measured strains and displacements at all angles of inclination. If all experimental observations from all inclination angles are considered as shown in Fig. 12, the FE model with micromechanics-based material properties provides excellent agreement with the experimental observations.

Figure 12 demonstrates the excellent agreement obtained between the micromechanics-based FE model results and the experimental observations for all inclination angles with slope = 0.999 and $R^2 =$

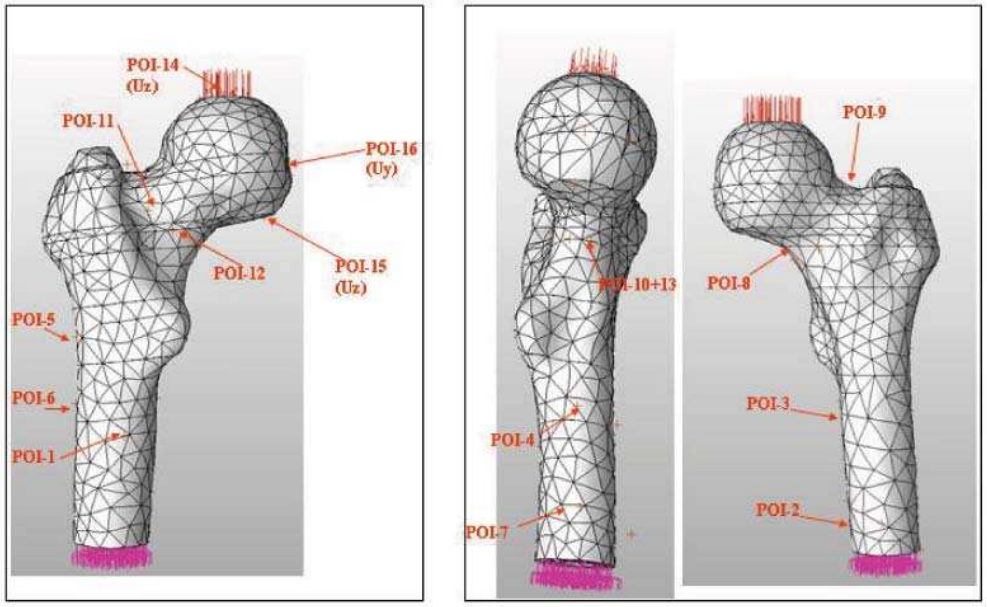

FIGURE 9. FE models and 16 POI for comparison purposes

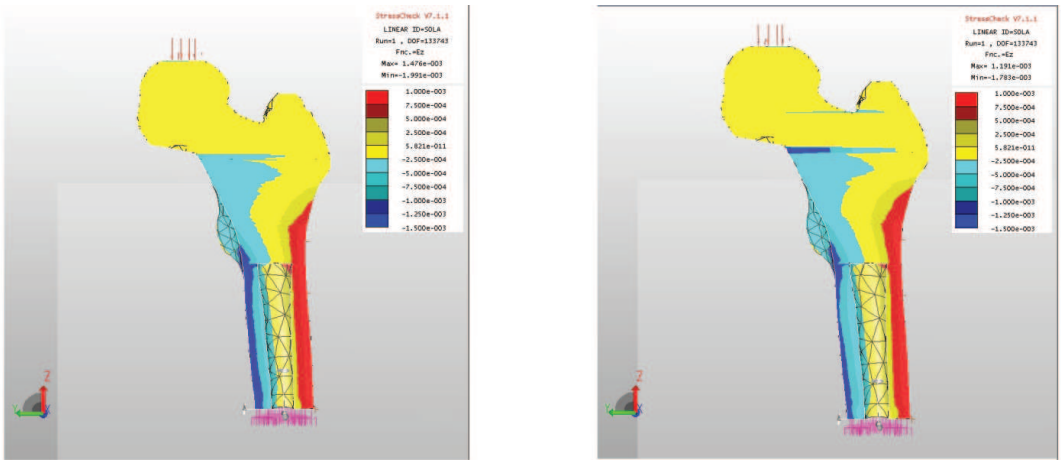

FIGURE 10. Variable ε_{zz} for the 0° inclination angle. Material properties assigned by two different strategies: Micromechanics-based (left) and empirically based (right)

0.96. This is slightly better compared to the best available empirically based FE models, that is, the ones of [12].

3.3 FE Results Using Transversely Isotropic Inhomogeneous Material Properties Compared to Experimental Observations

Preliminary FE analyses with micromechanics-based inhomogeneous transversely isotropic material properties in the cortical shaft region, and inhomogeneous isotropic material properties in the head region, were also performed. Comparison of these analyses with the experimental observations from all inclination angles are shown in Fig. 13.

Although it seems that the FE models with transversely isotropic material properties in the cortical region result in slightly poorer agreement with the experimental observations (compared to the isotropic case), slope = 1.014 and $R^2 = 0.92$, two points are to be realized: (1) The loading configuration on the bone induces mostly normal strains and displacements in the longitudinal direction (no shearing or torsion) and (2) the isotropic and transversely isotropic correlations are of comparable accuracy.

We anticipate that assigning orthotropic (or at least transversely isotropic) material properties to the (cortical and trabecular) bone material in the head region will produce the most accurate predictions compared to experimental observations, if the in vitro experiment applies not only a compression load on the head, but also torsional or shear type of loading. Because these kinds of experiments on fresh-frozen human femurs are unavailable at this stage, we will evaluate this hypothesis in a future investigation.

4. SUMMARY, CONCLUSIONS, AND PERSPECTIVES

This study is aimed at improving the methods presented in [5, 13], by generating more reliable FE models of the proximal femur using subject-specific QCT data and micromechanics-based determination of material properties (inhomogeneous isotropic and transversely isotropic). To the best of our knowledge, this work is the first to consider an inhomogeneous Poisson ratio and the first to compare results obtained by micromechanics-based material properties to experimental observations on a whole organ, and in particular, on the human femur.

By a systematic micromechanics-based method, we evaluated bone inhomogeneous isotropic and transversely isotropic properties (including Poisson ratios) from QCT scans. We first assigned to the p-

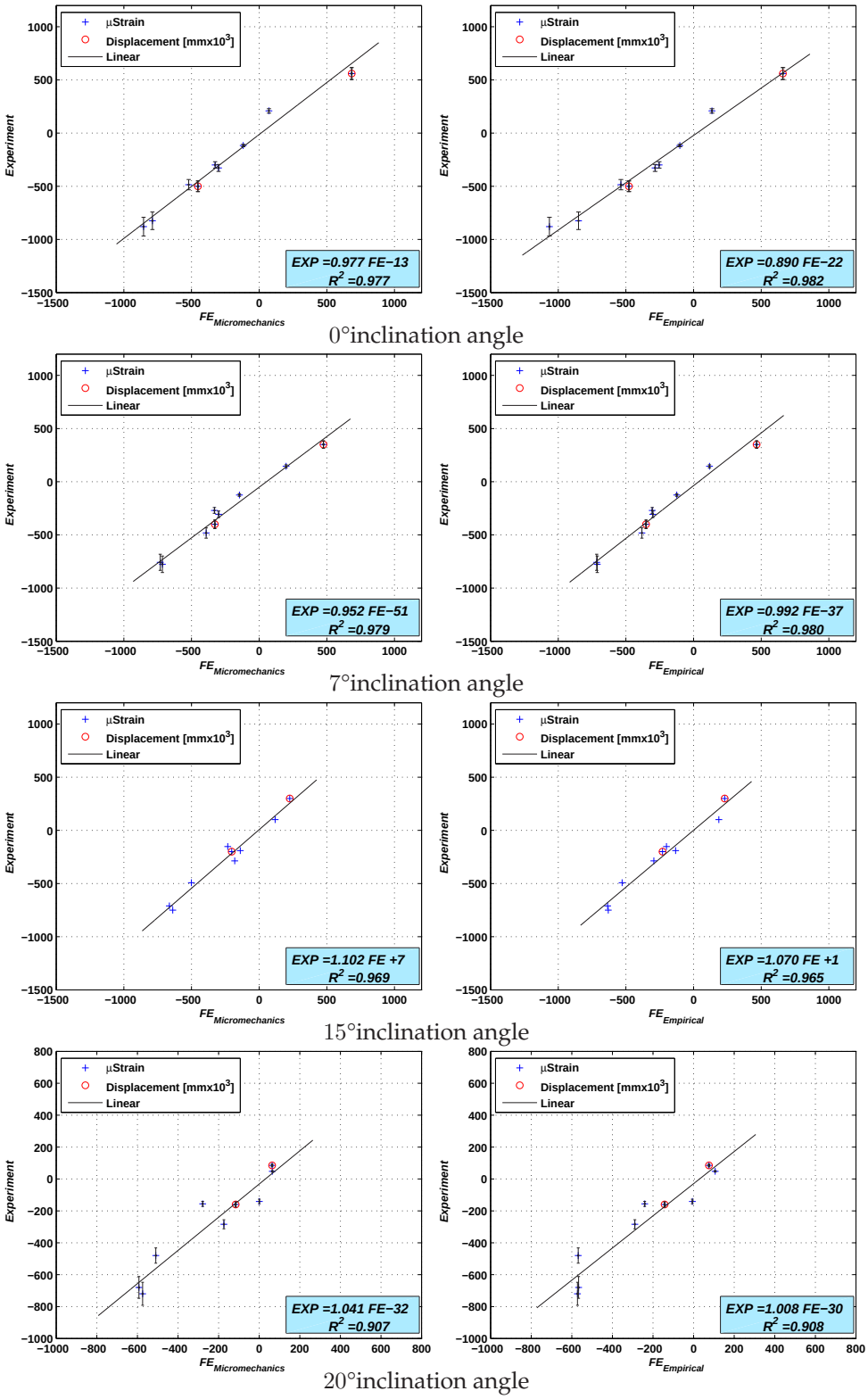

FIGURE 11. FE results (strains and displacements) compared to experimental observations. Material properties assigned by two different strategies: Micromechanics-based (left) and empirically based (right)

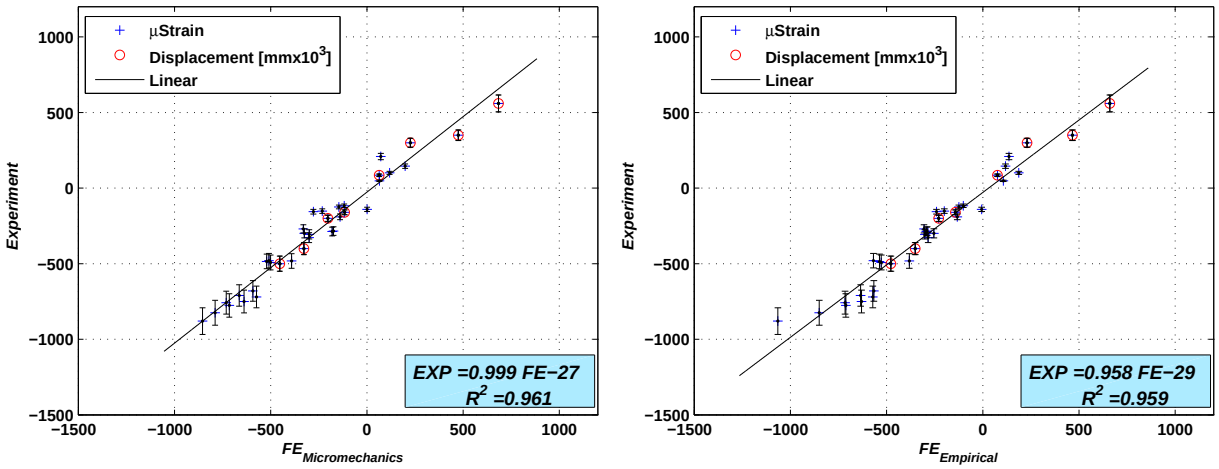

FIGURE 12. FE results (strains and displacements) compared to *all* experimental observations. Material properties assigned by two different strategies: Micromechanics-based (left) and empirically based (right)

FE model of the bone isotropic inhomogeneous material properties so that the Young modulus is the one associated with the longitudinal direction and the Poisson ratio is the one in the transverse direction. This is because the bone is loaded by compression, with the dominant mechanical response in the longitudinal direction. Similar FE analyses, but with an isotropic "best empirically based" Young modulus determined by Keyak and Falkinstein [12] and a constant Poisson ratio, validated in [5, 13], provide similar estimation of the longitudinal Young modulus compared to the micromechanics-based model and comparable strains and displacements.

The results of an in vitro experiment on a fresh-frozen femur were used to validate the p-FE simulations. Strains and displacements along the bone's surface for compressive loading on the femur's head at different inclination angles were used for the validation of the p-FE simulations. It was demonstrated that excellent predictions can be obtained. The agreement between the analyses and experiments are, to the best of the authors' knowledge, more accurate than other investigations reported in the literature.

Because only the micromechanics-based method may estimate the patient-specific anisotropic material properties for the bone and excellent correlation with experimental observations on the whole organ were realized, it is recommended to use a micromechanics-based method in conjunction with

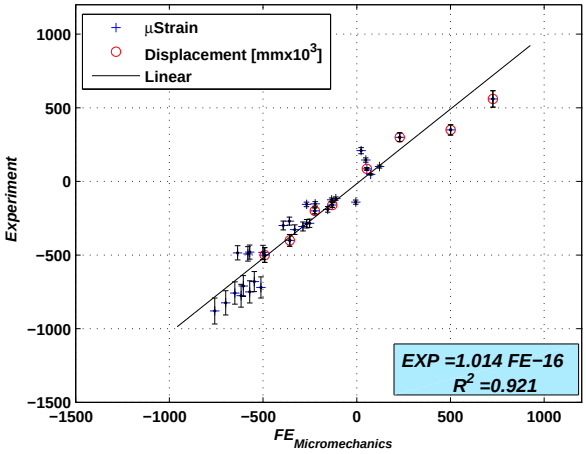

FIGURE 13. FE results (strains and displacements) compared to *all* experimental observations. Transversely isotropic cortical and isotropic head material properties assigned by a micromechanics-based model

p-FEMs for a subject-specific FE analysis of the femur.

Of course, also in both the cortical and the trabecular compartments of the head region, the bone material is anisotropic (orthotropic, or at least transversely isotropic at first approximation). This may be of major importance if one considers a more complicated state of stress on the bone involving shear and torsion. To this end, investigation of the

anisotropic material properties assigned to FE models of the human femur is currently under way and will be reported in a future publication. The principal material directions are to be determined based on structural considerations.

As a future step in this line of research, we strive to perform in vitro experiments under shear and torsional loadings to enhance the experimental database against which the micromechanics-based FE simulations can be compared to further validate our methods.

REFERENCES

1. Peng, L., Bai, J., Zeng, Z., and Zhou, Y., Comparison of isotropic and orthotropic material property assignments on femoral finite element models under two loading conditions. *Med. Eng. Phys.* **28**:227–233, 2006.
2. Schileo, E., Taddei, F., Malandrino, A., Cristofolini, L., and Viceconti, M., Subject-specific finite element models can accurately predict strain levels in long bones. *J. Biomech.* **40**:2982–2989, 2007.
3. Taddei, F., Schileo, E., Helgason, B., Cristofolini, L., and Viceconti, M., The material mapping strategy influences the accuracy of CT-based finite element models of bones: An evaluation against experimental measurements. *Med. Eng. Phys.* **29**:973–979, 2007.
4. Yosibash, Z., Padan, R., Joscowicz, L., and Milgrom, C., A CT-based high-order finite element analysis of the human proximal femur compared to in-vitro experiments. *ASME J. Biomech. Eng.* **129**:297–309, 2007.
5. Yosibash, Z., Trabelsi, N., and Milgrom, C., Reliable simulations of the human proximal femur by high-order finite element analysis validated by experimental observations. *J. Biomech.* **40**:3688–3699, 2007.
6. Helgason, B., Taddei, F., Palsson, F., Schileo, E., Cristofolini, L., Viceconti, M., and Brynjolfsson, S., A modified method for assigning material properties to FE models of bones. *Med. Eng. Phys.* **30**:444–453, 2008.
7. Lotz, J. C., Gerhart, T. N., and Hayes, W. C., Mechanical properties of trabecular bone from the proximal femur: A quantitative CT study. *J. Comput. Assisted Tomog.* **14**:107–114, 1990.
8. Lotz, J. C., Gerhart, T. N., and Hayes, W. C., Mechanical properties of metaphyseal bone in the proximal femur. *J. Biomech.* **24**:317–329, 1991.
9. Keaveny, T. M., Guo, E., Wachtel, E. F., McMahon, T. A., and Hayes, W. C., Trabecular bone exhibits fully linear elastic behavior and yields at low strains. *J. Biomech.* **27**:1127–1136, 1994.
10. Keller, T. S., Predicting the compressive mechanical behavior of bone. *J. Biomech.* **27**:1159–1168, 1994.
11. Wirtz D. C., Schiffers, N., Pandorf, T., Radermacher, K., Weichert, D., and Forst, R., Critical evaluation of known bone material properties to realize anisotropic FE-simulation of the proximal femur. *J. Biomech.* **33**:1325–1330, 2000.
12. Keyak, J. H., and Falkinstein, Y., Comparison of in situ and in vitro CT scan-based finite element model predictions of proximal femoral fracture load. *Med. Eng. Phys.* **25**:781–787, 2003.
13. Trabelsi, N., Yosibash, Z., and Milgrom, C., Validation of subject-specific automated p-FE analysis of the proximal femur. *J. Biomech.* 2008 in press, doi: 10.1016/j.jbiomech.2008.10.039.
14. Shahar, R., Zaslansky, P., Barak, M., Friesem, A. A., Currey, J. D., and Weiner, S., Anisotropic Poissons ratio and compression modulus of cortical bone determined by speckle interferometry. *J. Biomech.* **40**:252–264, 2007.
15. Hellmich, C., Kober, C., and Erdmann, B., Micromechanics-based conversion of CT data into anisotropic elasticity tensors, applied to FE simulations of a mandible. *Ann. Biomed. Eng.* **36**:108–122, 2008.
16. Fritsch, A., and Hellmich, C., Universal microstructural patterns in cortical and trabecular, extracellular and extravascular bone materials: Micromechanics-based prediction of anisotropic elasticity. *J. Theoret. Biol.* **244**:597–620, 2008.
17. Crawley, E. O., Evans, W. D., and Owen, G. M., A theoretical analysis of the accuracy of single-energy CT bone measurements. *Phys. Med. Biol.* **33**:1113–1127, 1988.
18. Hellmich, C., and Ulm, F.-J., Micro-porodynamics of bones: prediction of the 'Frenkel-Biot' slow compressional wave. *J. Eng.*

Mech. **131**:918–927, 2005.

19. Hellmich, C., Ulm, F.-J., and Dormieux, L., Can the diverse elastic properties of trabecular and cortical bone be attributed to only a few tissue-independent phase properties and their interactions? *Biomech. Model. Mechanobiol.* **2**:219–238, 2004.
20. Jackson, D. F., and Hawkes,D. J., X-ray attenuation coefficients of elements and mixtures. *Phys. Lett.* **70**:169–233, 1981.
21. Biltz, R. M., and Pellegrino, E. D., The chemical anatomy of bone. *J. Bone Joint Surgery.* **51-A**:456–466, 1969.
22. Lees, S., Considerations regarding the structure of the mammalian mineralized osteoid from viewpoint of the generalized packing model. *Connective Tissue Res.* **16**:281–303, 1987.
23. Lees, S., Heeley, J. D., and Cleary, P. F., A study of some properties of a sample of bovine cortical bone using ultrasound. *Calcified Tissue Int.* **29**:107–117, 1979.
24. Lees, S., Hanson, D., and Page,E. A., Some acoustical properties of the otic bones of a fin whale. *J. Acoust. Soc. Am.* **99**:2421–2427, 1995.
25. Boivin, G. and Meunier, P. J., The degree of mineralization of bone tissue measured by computerized quantitative contact microradiography. *Calcified Tissue Int.* **70**:503–511, 2002.
26. Roschger, P., Gupta, H. S., Berzlanovich, A., Ittner, G., Dempster, D. W., Fratzl, P., Cosman, F., Parisien, M., Lindsay, R., Nieves, J. W., and Klaushofer, K., Constant mineralization density distribution in cancellous human bone. *Bone.* **32**:316–323, 2003.
27. Akkus, O., Polyakova-Akkus, A., Adar, F., and Schaffler, M. B., Aging of microstructural compartments in human compact bone. *J. Bone Min. Res.* **18**:1012–1019, 2003.
28. Bossy, E., Talmant, M., Peyrin, F., Akrout, L., Cloetens, P., and Laugier,P., In vitro study of the ultrasonic axial transmission technique at the radius: 1 MHz velocity measurements are sensitive to both mineralization and introcortical porosity. *J. Bone Min. Res.* **19**:1548–1556, 2004.
29. Gould, S. J., and Lewontin, R. C., The spandrels of San Marco and the Panglossian paradigm: A critique of the adaptionist program. *Proc. R. Soc. London, Ser. B.* **205**:581–598, 1979.
30. Ashman, R. B., Cowin, S. C., van Buskirk, W. C., and Rice, J. C., A continuous wave technique for the measurement of the elastic properties of cortical bone. *J. Biomech.* **17**:349–361, 1984.
31. Bilaniuk, N., and Wong, G. S. K., Speed of sound in pure water as a function of temperature. *J. Acoust. Soc. Am.* **93**:1609–1612, 1993.
32. Lees, S., Ahern, J. M., and Leonard, M., Parameters influencing the sonic velocity in compact calcified tissues of various species. *J. Acoust. Soc. Am.* **74**:28–33, 1983.
33. Lees, S., Tao, N.-J., and Lindsay, M., Studies of compact hard tissues and collagen by means of Brillouin light scattering. *Connective Tissue Res.* **24**:187–205, 1990.
34. Turner, C. H., Rho, J.-Y., Takano, Y., Tsui, T. Y., and Pharr, G. M., The elastic properties of cortical and trabecular bone tissues are similar: Results from two microscopic measurement techniques. *J. Biomech.* **32**:437–441, 1999.
35. Rho, J.-Y., Mishra, S. R., Chung, K., Bai, J., and Pharr, G. M., Relationship between ultrastructure and the nanoindentation properties of intramuscular herring bones. *Ann. Biomed. Eng.* **29**:1–7, 2001.
36. Swadener, J. G., Rho, J.-Y., and Pharr, G. M., Effects of anisotropy on elastic moduli measured by nanoindentation in human tibial cortical bone. *J. Biomed. Mater. Res.* **57**:108–112, 2001.
37. Zaoui, A., Continuum micromechanics: Survey. *J. Eng. Mech.* **128**:808–816, 2002.
38. Mori, T., and Tanaka, K., Average stress in matrix and average elastic energy of materials with misfitting inclusions. *Acta Metall.* **21**:571–574, 1973.
39. Benveniste, Y., A new approach to the application of Mori-Tanakas theory in composite materials. *Mech. Mater.* **6**:147–157, 1987.
40. Fritsch, A., Dormieux, L., and Hellmich, C., Porous polycrystals built up by uniformly and axisymmetrically oriented needles: Homogenization of elastic properties. *Comptes Rendus Mécanique.* **334**:151–157, 2006.
41. Laws, N., The determination of stress and strain concentrations at an ellipsoidal inclusion in an anisotropic material. *J. Elasticity.* **7**:91–97,

1977.
42. Yoon, Y. J., Yang, G., and Cowin, S. C., Estimation of the effective transversely isotropic elastic constants of a material from known values of the material's orthotropic elastic constants. *Biomech. Model. Mechanobiol.* **1**:83–93, 2002.
43. Kober, C., Erdmann, B., Hellmich, C., Sader, R., and Zeilhofer, H.-F., Consideration of anisotropic elasticity minimizes volumetric rather than shear deformation in human mandible. *Comput. Methods Biomech. Biomed. Eng.* **9**:91–101, 2006.